PUBLISHED BY THE AMERICAN CHEMICAL SOCIETY

analytical chemistry

January 15, 2008

407
Atmospheric Pressure IR MALDI Imaging MS for Plant Metabolomics

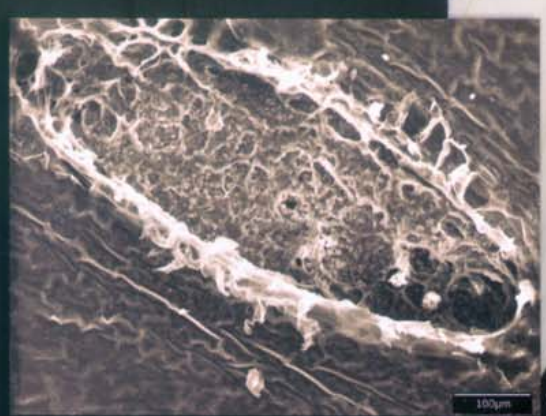

369
Microfluidic Whole-Chip Temperature Measurement with Thin-Film PDMS/Rhodamine B

437
Molecular Imprinting at Walls of Silica Nanotubes for TNT Recognition

http://pubs.acs.org/ac

Anal. Chem. **2008,** *80,* 407−420

Atmospheric Pressure Infrared MALDI Imaging Mass Spectrometry for Plant Metabolomics

Yue Li, Bindesh Shrestha, and Akos Vertes*

Department of Chemistry, W. M. Keck Institute for Proteomics Technology and Applications, George Washington University, Washington, D.C. 20052

The utility of atmospheric pressure infrared MALDI mass spectrometry (AP IR-MALDI) was assessed for plant metabolomics studies. Tissue sections from plant organs, including flowers, ovaries, aggregate fruits, fruits, leaves, tubers, bulbs, and seeds were studied in both positive and negative ion modes. For leaves, single laser pulses sampled the cuticle and upper epidermal cells, whereas multiple pulses were demonstrated to ablate some mesophyll layers. Tandem mass spectra were obtained with collision-activated dissociation to aid with the identification of some observed ions. In the positive mode, most ions were produced as potassium, proton, or sometimes sodium ion adducts, whereas proton loss was dominant in the negative ion mode. Over 50 small metabolites and various lipids were detected in the spectra including, for example, 7 of the 10 intermediates in the citric acid cycle. Key components of the glycolysis pathway occurring in the plant cytosol were found along with intermediates of phospholipid biosynthesis and reactants or products of amino acid, nucleotide, oligosaccharide, and flavonoid biosynthesis. AP IR-MALDI mass spectrometry was used to follow the fluid transport driven by transpiration and image the spatial distributions of several metabolites in a white lily (*Lilium candidum*) flower petal.

It is estimated that ~200 000 metabolites exist in the plant kingdom. These metabolites play a critical role in biological function, such as energy production and the biosynthesis of macromolecules.[1,2] Knowledge of the structure, function, and biosynthetic pathways for metabolites in plants is important for various areas including energy production, agriculture, environmental processes, and pharmacology.

Due to the diversity of metabolites, numerous methods have been developed to offer both the necessary selectivity and sensitivity for their analysis in highly complex mixtures. These include mass spectrometry (MS),[3−5] nuclear magnetic resonance,[6,7] and vibrational (IR or Raman) spectroscopy[8−10] coupled with separation techniques, including gas chromatography (GC),[11] liquid chromatography (LC),[12] and capillary electrophoresis (CE).[4,13] Often complementary information from several techniques is used for the identification and/or quantitation of metabolites. The analytical techniques used in the emerging field of metabolomics have recently been reviewed.[14]

Due to its inherently high sensitivity and molecular specificity, mass spectrometry has become an increasingly important tool for the analysis of biological systems. Several hyphenated approaches, such as GC/MS, LC/MS, and CE/MS, were developed to enable better metabolite identification and quantitation.[1,15−23] In combination with soft ionization methods such as electrospray ionization (ESI) and matrix-assisted laser desorption/ionization (MALDI), mass spectrometry proved to be useful in the investigation of biological systems.[24−27] In particular, ESI mass spectrometry was widely applied in the investigation of primary and secondary plant

* To whom correspondence should be addressed. E-mail: vertes@gwu.edu.

(1) Lisec, J.; Schauer, N.; Kopka, J.; Willmitzer, L.; Fernie, A. R. *Nat. Protoc.* **2006**, *1*, 387−396.
(2) Wink, M. *Theor. Appl. Genet.* **1988**, *75*, 225−233.
(3) Wilson, I. D.; Plumb, R.; Granger, J.; Major, H.; Williams, R.; Lenz, E. M. *J. Chromatogr. B-Anal. Technol. Biomed. Life Sci.* **2005**, *817*, 67−76.
(4) Soga, T.; Ohashi, Y.; Ueno, Y.; Naraoka, H.; Tomita, M.; Nishioka, T. *J. Proteome Res.* **2003**, *2*, 488−494.
(5) Glinski, M.; Weckwerth, W. *Mass Spectrom. Rev.* **2006**, *25*, 173−214.
(6) Solanky, K. S.; Bailey, N. J. C.; Beckwith-Hall, B. M.; Davis, A.; Bingham, S.; Holmes, E.; Nicholson, J. K.; Cassidy, A. *Anal. Biochem.* **2003**, *323*, 197−204.
(7) Terskikh, V. V.; Feurtado, J. A.; Borchardt, S.; Giblin, M.; Abrams, S. R.; Kermode, A. R. *J. Exp. Bot.* **2005**, *56*, 2253−2265.
(8) Johnson, H. E.; Broadhurst, D.; Kell, D. B.; Theodorou, M. K.; Merry, R. J.; Griffith, G. W. *Appl. Environ. Microbiol.* **2004**, *70*, 1583−1592.
(9) Johnson, H. E.; Broadhurst, D.; Goodacre, R.; Smith, A. R. *Phytochemistry* **2003**, *62*, 919−928.
(10) Jarvis, R. M.; Goodacre, R. *FEMS Microbiol. Lett.* **2004**, *232*, 127−132.
(11) Roessner-Tunali, U.; Hegemann, B.; Lytovchenko, A.; Carrari, F.; Bruedigam, C.; Granot, D.; Fernie, A. R. *Plant Physiol.* **2003**, *133*, 84−99.
(12) Plumb, R.; Granger, J.; Stumpf, C.; Wilson, I. D.; Evans, J. A.; Lenz, E. M. *Analyst* **2003**, *128*, 81
(13) Sato, S.; Soga, T.; Nishioka, T.; Tomita, M. *Plant J.* **2004**, *40*, 151−163.
(14) Dunn, W. B.; Bailey, N. J. C.; Johnson, H. E. *Analyst* **2005**, *130*, 606−625.
(15) Roessner, U.; Wagner, C.; Kopka, J.; Trethewey, R. N.; Willmitzer, L. *Plant J.* **2000**, *23*, 131−142.
(16) Tolstikov, V. V.; Lommen, A.; Nakanishi, K.; Tanaka, N.; Fiehn, O. *Anal. Chem.* **2003**, *75*, 6737−6740.
(17) Edwards, E. L.; Rodrigues, J. A.; Ferreira, J.; Goodall, D. M.; Rauter, A. P.; Justino, J.; Thomas-Oates, J. *Electrophoresis* **2006**, *27*, 2164−2170.
(18) Wolfender, J.; Ndjoko, K.; Hostettmann, K. *J. Chromatogr., A* **2003**, *1000*, 437−455.
(19) Garratt, L. C.; Linforth, R.; Taylor, A.; Lowe, K. C.; Power, J. B.; Davey, M. R. *Plant Biotechnol. J.* **2005**, *3*, 165−174.
(20) Zhou, R.; Squires, T. M.; Ambrose, S. J.; Abrams, S. R.; Ross, A. R. S.; Cutler, A. J. *J. Chromatogr., A* **2003**, *1010*, 75−85.
(21) Fiehn, O.; Kopka, J.; Threthewey, R. N.; Willmitzer, L. *Anal. Chem.* **2000**, *72*, 3573−3580.
(22) Keurentjes, J. J. B.; Fu, J.; Ric, de Vos, C. H.; Lommen, A.; Hall, R. D.; Bino, R. J.; van der Plas, L. H. W.; Jansen, R. C.; Vreugdenhil, D.; Koornneef, M. *Nat. Genet.* **2006**, *38*, 842−849.
(23) El-Zohri, M. H. A.; Cabala, R.; Frank, H. *Anal. Bioanal. Chem.* **2005**, *382*, 1871−1876.
(24) Fenselau, C. *Anal. Chem.* **1997**, *69*, A661−A665.

10.1021/ac701703f CCC: $40.75 © 2008 American Chemical Society
Published on Web 12/19/2007

metabolites;[28−32] e.g., citric acid, hexose sugars, and malic acid were found in tomatos.[33] In these ESI studies, however, the plant tissues had to be extracted by solvents through laborious procedures.

Sample preparation protocols for the conventional MALDI analysis of plant metabolites usually start with extraction followed by mixing the extract with a matrix solution. In imaging MALDI experiments, it is possible to directly analyze tissue sections; however, the sample surface needs to be uniformly covered with the matrix without significantly altering the original molecular distributions. This task is particularly challenging in the case of water-soluble analytes and small molecules. Moreover, for analysis, the matrix-treated samples have to be transferred into the vacuum system of the mass spectrometer. These delicate and laborious procedures considerably restrict the choice of samples and exclude the possibility of in vivo studies.

Conventional MALDI relies on a UV laser to generate ions. Although infrared (IR) MALDI had been demonstrated to produce intact ions of large nucleic acids and work with ice as a matrix,[34,35] due to its less robust analytical performance relative to UV-MALDI (primarily the lower sensitivity for peptides and proteins) and to the lack of low-cost mid-IR laser sources, it has not been universally embraced by the analytical community. However, certain advantages of IR-MALDI make it attractive in certain applications. First, many molecules have a strong absorption in the mid-IR spectral region; thus, there are more potential matrixes for IR-MALDI. Second, IR-MALDI can be directly coupled with some liquid-phase separation techniques.[36−39] Importantly, Laiko et al.[40,41] successfully used liquid water as a matrix with a 3-μm IR laser at atmospheric pressure to generate peptide ions. As water is a major native component of biological systems, direct ion production from biomolecules in an aqueous environment opens new possibilities for the in vivo analysis of biochemical processes, e.g., in tissues and cell cultures.[42,43]

The information on the spatial distribution and temporal variations of chemical species in living organisms is essential to the understanding of complex biological phenomena. Molecular imaging based on mass spectrometry has attracted extensive interest for over two decades because of its excellent sensitivity and the ability to uniquely identify unknown chemical species.[44−49] There are significant efforts underway to improve molecular imaging technologies based on MALDI mass spectrometry.[50−54] The combination of MALDI imaging with confocal microscopy has led to lateral resolution (~0.6 μm with 337-nm laser light) close to the diffraction limit and to rapid image acquisition (up to 50 pixels/s).[55]

In the low-mass range, imaging by conventional vacuum MALDI is complemented by secondary ion mass spectrometry (SIMS)[45,56,57] that produces excellent (submicrometer) spatial resolution for these analytes. With SIMS, thousands of spectra can be obtained from a 20-μm-diameter mammalian cell, and as little as 40 zmol of an analyte can be detected from the surface of a typical eukaryotic cell.[58] The sensitivity for high-mass ions (m/z > 1000), however, is limited due to low secondary ion yields[59] as well as low detection efficiencies in current SIMS instrumentation.[60] In contrast, MALDI mass spectrometry can typically analyze molecules up to 100 kDa but the sensitivity for IR-MALDI is only in the low-femtomole range. Although IR-MALDI in general is considered less sensitive than UV IR-MALDI, this statement is too broad. While the sensitivity of IR-MALDI for proteins is certainly lower than that of UV-MALDI, the relationship is reversed for nucleic acids. The need for a vacuum environment in both SIMS and MALDI prevents their use in in vivo imaging experiments.

Some of the recently emerging atmospheric pressure (AP) ion sources, such as desorption electrospray ionization (DESI),[61,62] AP IR-MALDI,[42] and laser ablation electrospray ionization (LAESI),[63] have also demonstrated imaging capabilities. DESI was applied to obtain images of specific lipids in intact rat brain tissue,[64]

(25) Kahn, M. L.; Parra-Colmenares, A.; Ford, C. L.; Kaser, F.; McCaskill, D.; Ketchum, R. E. *Anal. Biochem.* **2002**, *307*, 219−225.
(26) Allen, J.; Davey, H. M.; Broadhurst, D.; Heald, J. K.; Rowland, J. J.; Oliver, S. G.; Kell, D. B. *Nat. Biotechnol.* **2003**, *21*, 692−696.
(27) Li, L.; Garden, R. W.; Sweedler, J. V. *Trends Biotechnol.* **2000**, *18*, 151−160.
(28) Dunn, W. B.; Overy, S.; Quick, W. P. *Metabolomics* **2005**, *1*, 137−148.
(29) Goodacre, R.; Vaidyanathan, S.; Bianchi, G.; Kell, D. B. *Analyst* **2002**, *127*, 1457−1462.
(30) Wang, X.; Li, W.; Li, M.; Welti, R. *Physiol. Plant.* **2006**, *126*, 90−96.
(31) Welti, R.; Li.W.; Li, M.; Sang, Y.; Biesiada, H.; Zhou, H.; Rajashekar, C. B.; Williams, T. D.; Wang, X. *J. Biol. Chem.* **2002**, *277*, 31994−32002.
(32) Welti, R.; Wang, X.; Williams, T. D. *Anal. Biochem.* **2003**, *314*, 149−152.
(33) Overy, S. A.; Walker, H. J.; Malone, S.; Howard, T. P.; Baxter, C. J.; Sweetlove, L. J.; Hill, S. A.; Quick, W. P. *J. Exp. Bot.* **2005**, *56*, 287−296.
(34) Berkenkamp, S.; Kirpekar, F.; Hillenkamp, F. *Science* **1998**, *281*, 260−262.
(35) Berkenkamp, S.; Karas, M.; Hillenkamp, F. *Proc. Natl. Acad. Sci. U.S.A.* **1996**, *93*, 7003−7007.
(36) Daniel, J. M.; Laiko, V. V.; Doroshenko, V. M.; Zenobi, R. *Anal. Bioanal. Chem.* **2005**, *383*, 895−902.
(37) Daniel, J. M.; Ehala, S.; Friess, S. D.; Zenobi, R. *Analyst* **2004**, *129*, 574−578.
(38) Xu, Y. C.; Little, M. W.; Murray, K. K. *J. Am. Soc. Mass Spectrom.* **2006**, *17*, 469−474.
(39) Lawson, S. J.; Murray, K. K. *Rapid Commun. Mass Spectrom.* **2000**, *14*, 129−134.
(40) Laiko, V. V.; Taranenko, N. I.; Berkout, V. D.; Yakshin, M. A.; Prasad, C. R.; Lee, H. S.; Doroshenko, V. M. *J. Am. Soc. Mass Spectrom.* **2002**, *13*, 354−361.
(41) Laiko, V. V.; Taranenko, N. I.; Doroshenko, V. M. *J. Mass Spectrom.* **2006**, *41*, 1315−1321.
(42) Li, Y.; Shrestha, B.; Vertes, A. *Anal. Chem.* **2007**, *79*, 523−532.
(43) Dreisewerd, K.; Draude, F.; Kruppe, S.; Rohlfing, A.; Berkenkamp, S.; Pohlentz, G. *Anal. Chem.* **2007**, *79*, 4514−4520.
(44) Ostrowski, S. G.; Van Bell, C. T.; Winograd, N.; Ewing, A. G. *Science* **2004**, *305*, 71−73.
(45) Pacholski, M. L.; Winograd, N. *Chem. Rev.* **1999**, *99*, 2977−3005.
(46) Todd, P. J.; Schaaff, T. G.; Chaurand, P.; Caprioli, R. M. *J. Mass Spectrom.* **2001**, *36*, 355−369.
(47) McPhail, D. S. *J. Mater. Sci.* **2006**, *41*, 873−903.
(48) Rubakhin, S. S.; Jurchen, J. C.; Monroe, E. B.; Sweedler, J. V. *Drug Discovery Today* **2005**, *10*, 823−837.
(49) Caldwell, R. L.; Caprioli, R. M. *Mol. Cell. Proteomics* **2005**, *4*, 394−401.
(50) Jurchen, J. C.; Rubakhin, S. S.; Sweedler, J. V. *J. Am. Soc. Mass Spectrom.* **2005**, *16*, 1654−1659.
(51) Crecelius, A. C.; Cornett, D. S.; Caprioli, R. M.; Williams, B.; Dawant, B. M.; Bodenheimer, B. *J. Am. Soc. Mass Spectrom.* **2005**, *16*, 1093−1099.
(52) Luxembourg, S. L.; Mize, T. H.; McDonnell, L. A.; Heeren, R. M. A. *Anal. Chem.* **2004**, *76*, 5339−5344.
(53) Crossman, L.; McHugh, N. A.; Hsieh, Y. S.; Korfmacher, W. A.; Chen, J. W. *Rapid Commun. Mass Spectrom.* **2006**, *20*, 284−290.
(54) Lemaire, R.; Tabet, J. C.; Ducoroy, P.; Hendra, J. B.; Salzet, M.; Fournier, I. *Anal. Chem.* **2006**, *78*, 809−819.
(55) Spengler, B.; Hubert, M. *J. Am. Soc. Mass Spectrom.* **2002**, *13*, 735−748.
(56) Winograd, N. *Appl. Surf. Sci.* **2003**, *203*, 13−19.
(57) Belu, A. M.; Graham, D. J.; Castner, D. G. *Biomaterials* **2003**, *24*, 3635−3653.
(58) Quong, J. N.; Knize, M. G.; Kulp, K. S.; Wu, K. J. *Appl. Surf. Sci.* **2004**, *231−232*, 424−427.
(59) Adriaensen, L.; Vangaever, F.; Lenaerts, J.; Gijbels, R. *Rapid Commun. Mass Spectrom.* **2005**, *19*, 1017−1024.
(60) Gilmore, I. S.; Seah, M. P. *Int. J. Mass Spectrom.* **2000**, *202*, 217−229.

AP IR-MALDI produced images of metabolites in fruit tissue sections, whereas LAESI was used to generate spatial profiles of metabolites in a French marigold seedling. Both DESI and LAESI showed analytical capabilities up to 66 kDa and a spatial resolution of ~300 μm. In contrast, using oversampling, a spatial resolution of 40 μm was obtained for AP IR-MALDI, but the high-mass limit for this method appeared to be at 3 kDa.

Keeping the sample at atmospheric pressure for MALDI mass spectrometry[65−67] offers unique advantages in some applications.[68−70] Despite its slightly lower sensitivity compared to its vacuum counterpart (for carbohydrates, 3-fmol sensitivity was demonstrated for AP IR-MALDI), due to the reduced sample handling and the possibility to use a broader class of matrixes (including liquids), AP MALDI is expected to play a role in, for example, in vivo studies.

Recently, we reported AP IR-MALDI imaging using a modified commercial Q-TOF mass spectrometer.[42] Native water in plant tissues was demonstrated to serve as an efficient matrix for positive ion production with IR laser irradiation. We applied this approach to map the spatial distributions of peptides on surfaces and of several small molecules in biological tissues without the addition of an external matrix. Here we report on AP IR-MALDI experiments with diverse plant tissues in both positive and negative ion modes as well as on imaging results for fluid transport induced by plant transpiration. The main aim of this study was to demonstrate the ability of the AP IR-MALDI technique to identify and image a wide variety of metabolites in plants and to gauge its potential for in vivo investigations.

EXPERIMENTAL SECTION

Mass Spectrometer and Laser. The instrument has been described in detail in a previous publication;[42] thus, only a brief overview is provided here. A home-built AP MALDI ion source with a 30-mm-long inlet capillary (i.d. = 127 μm) was mounted on a Q-TOF Premier mass spectrometer (Waters Co., Milford, MA). An optical parametric oscillator converted the output of a 10-Hz repetition rate Nd:YAG laser to mid-IR pulses of 4-ns duration at 2940-nm wavelength. Beam steering and focusing were accomplished by gold mirrors and a 50-mm focal length plano-convex lens, respectively. The laser beam with an ~45° incidence angle was focused into an elliptical laser spot of ~250-μm average diameter (measured by optical microscopy of burn patterns on photographic paper). The laser pulse energy at the target was measured to be 150 μJ, which for the given focusing conditions corresponded to a fluence of 0.3 J/cm^2. To characterize material removal by the laser, some the ablation craters were imaged by a scanning electron microscope (SEM) (JEOL JSM-840A, Peabody, MA). The distance between the mass spectrometer inlet orifice and the sample surface was set to ~2 mm to maximize the ion signal intensity without producing an electrical breakdown. Positive and negative ion spectra were collected for all samples. In order to identify particular ions, tandem mass spectrometry was used. The fragments were produced by collision-activated dissociation (CAD) in argon collision gas with a typical pressure of 4×10^{-3} mbar and with a collision energy set between 10 and 50 eV.

The laser-produced ions were collected by the AP interface using pulsed dynamic focusing[71] that provided a factor of 5 gain in ion abundances.[42] Under typical experimental conditions, the initial high voltages applied on the stainless steel target plate were +3.0 and −3.0 kV, and the voltages on the interface block were set to −50 and +50 V for positive and negative ions, respectively. The temperature of the interface block was held at 50 °C. Based on a series of dilution experiments, the sensitivity of the system was estimated to be ~1 fmol/pixel.

Identification of Ions. Due to the inherent complexity of the plant samples, identification of the ions based on their nominal mass alone is not possible. In order to elucidate the structure of the detected ions, we performed accurate mass measurements, isotope distribution analysis, and in some cases CAD for the comparison of fragmentation patterns. Accurate mass measurements were performed using internal calibration based on common ions that were known to be produced from plant samples. These included potassiated sugars, their clusters, and some organic acids. The mass accuracies for $m/z < 195$, $195 < m/z < 800$ and $800 < m/z < 1500$ are within ±0.012, ±0.049, and ±0.005, respectively. This enabled the selection of a short list of compounds for every peak using the AraCyc 3.5 metabolic pathways database at TAIR— The Arabidopsis Information Resource: http://www.arabidopsis.org/ for *Arabidopsis thaliana* (accessed June 7, 2007). Some assignments were made using the broader MetaCyc[72] combined database for 261 organisms at http://biocyc.org/ (accessed August 4, 2007). Lipid assignments were aided by the LIPID Metabolites and Pathways Strategy database maintained by the LIPID MAPS consortium. The database was accessed on August 6, 2007, at http://www.lipidmaps.org/.

Individual peak assignments were further aided by the comparison of M + n peak intensities to the calculated patterns obtained from the abundances of natural isotopes. Most of the product ions in the positive mode were formed through protonation or alkalination, whereas in the negative mode, deprotonation was dominant. As most plant tissues have a high concentration of potassium,[73] potassiated ions were more common than sodiated ones. In the potassiated ions, the natural isotope pattern for ^{39}K, ^{40}K, and ^{41}K (100, 0.01, and 7.22%, respectively) was superimposed on the M, M + 1, and M + 2 abundances stemming from the carbon isotope distributions and protonation. In the case of relatively small organic ions, with no protonation present, the

(61) Mulligan, C. C.; Talaty, N.; Cooks, R. G. *Chem. Commun.* **2006**, 1709−1711.
(62) Ifa, D. R.; Wiseman, J. M.; Song, Q.; Cooks, R. G. *Int. J. Mass Spectrom.* **2007**, *259*, 8−15.
(63) Nemes, P.; Vertes, A. *Anal. Chem.* **2007**, *79*, 8098−8106.
(64) Wiseman, J. M.; Ifa, D. R.; Song, Q.; Cooks, R. G. *Angew. Chem., Int. Ed.* **2006**, *45*, 7188−7192.
(65) Laiko, V. V.; Baldwin, M. A.; Burlingame, A. L. *Anal. Chem.* **2000**, *72*, 652−657.
(66) Callahan, J. H.; Galicia, M. C.; Vertes, A. *Appl. Surf. Sci.* **2002**, *197−198*, 130−137.
(67) Moyer, S. G.; Cotter, R. J. *Anal. Chem.* **2002**, *74*, 468A−476A.
(68) Zhang, J. H.; LaMotte, L. T.; Dodds, E. D.; Lebrilla, C. B. *Anal. Chem.* **2005**, *77*, 4429−4438.
(69) Hanton, S. D.; Parees, D. M.; Zweigenbaum, J. *J. Am. Soc. Mass Spectrom.* **2006**, *17*, 453−458.
(70) Creaser, C. S.; Ratcliffe, L. *Curr. Anal. Chem.* **2006**, *2*, 9−15.
(71) Tan, P. V.; Laiko, V. V.; Doroshenko, V. M. *Anal. Chem.* **2004**, *76*, 2462−2469.
(72) Caspi, R.; Foerster, H.; Fulcher, C. A.; Hopkinson, R.; Ingraham, J.; Kaipa, P.; Krummenacker, M.; Paley, S.; Pick, J.; Rhee, S. Y.; Tissier, C.; Zhang, P. F.; Karp, P. D. *Nucleic Acids Res.* **2006**, *34*, D511−D516.
(73) http://www.nal.usda.gov.

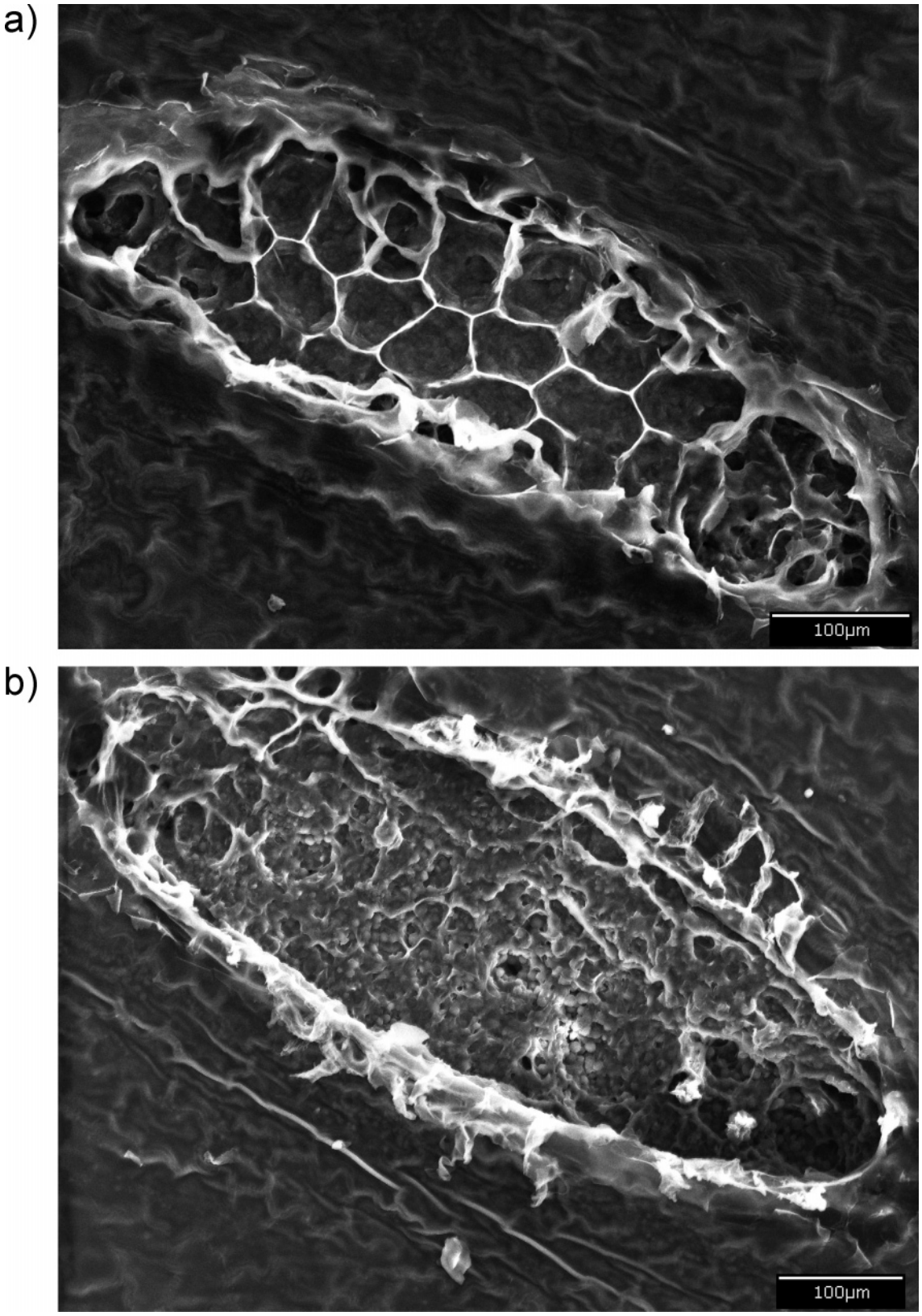

Figure 1. SEM images of ablation craters created by (a) a single and (b) six laser pulses of 0.27 ± 0.03 J/cm^2 fluence each, impinging on the upper surface of a peace lily plant (*Spathiphyllium*) leaf. After a single laser pulse, the tissue damage is localized to an elliptical area with 180 and 640 μm for the small and large axes, respectively. The top waxy cuticle layer and part of the upper epidermal cells were removed, but no damage to the underlying tissue was apparent. Upon exposure to six laser pulses, the laser crater became slightly larger (230 μm by 720 μm), and some of the palisade and spongy mesophyll was also removed.

higher intensity of the M + 2 ion compared to M + 1 was an indication of the presence of potassium. For high-fidelity structure assignments, the fragmentation patterns due to CAD in tandem mass spectra were compared to the corresponding spectra in the

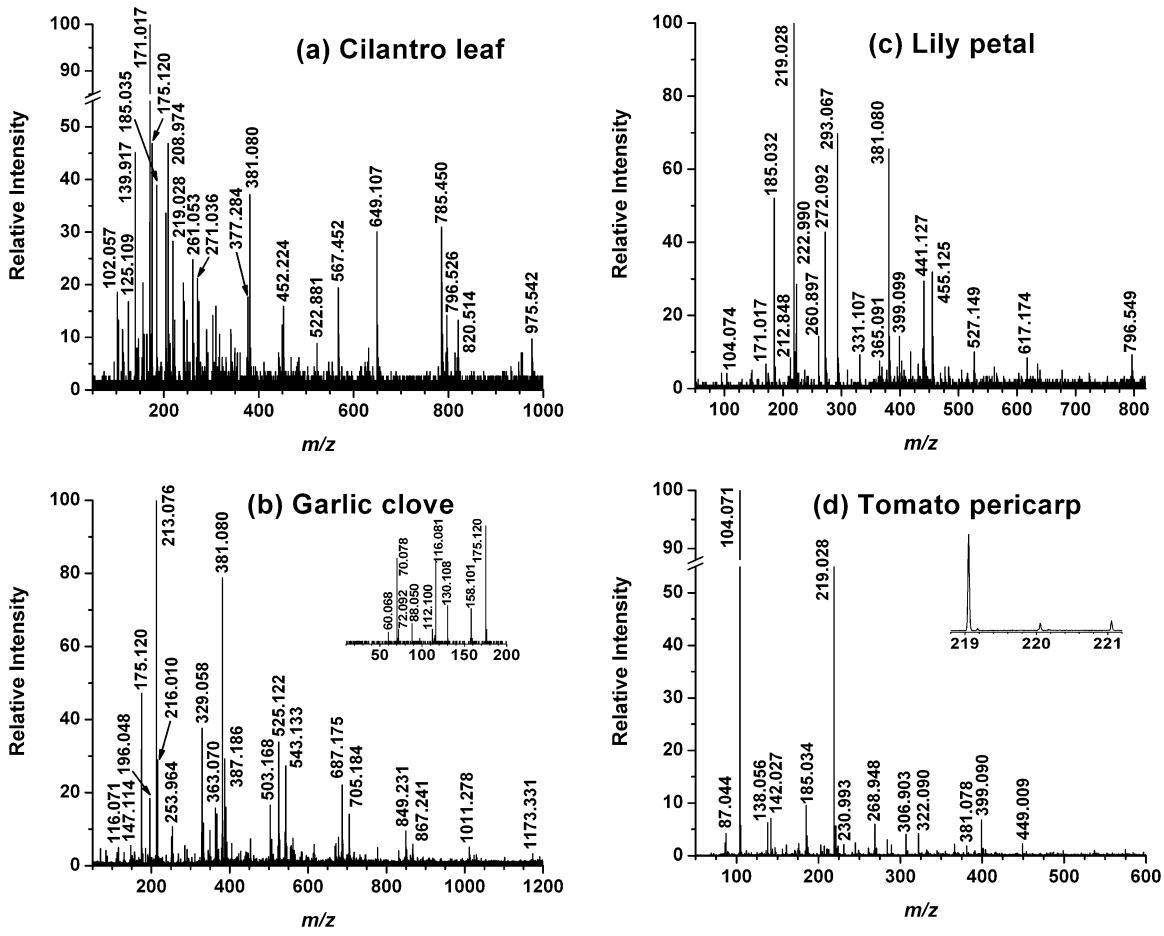

Figure 2. AP IR-MALDI mass spectra obtained in the positive ion mode from (a) the lamina of a cilantro leaf; (b) garlic bulb sections that exposed the storage tissue in the expanded leaf bases; (c) a segment of a white lily flower petal; and (d) sections of the outer wall of the pericarp of a tomato fruit. The inset in panel b shows the tandem mass spectrum of the *m*/*z* 175 ion that corresponds to protonated arginine. The isotopic distribution pattern for the *m*/*z* 219 ion in the inset of panel d is consistent with the presence of potassium.

NIST library (NIST Mass Spectral Search Program for the NIST/EPA/NIH Mass Spectral Library, Version 2.0). Even with the combination of the three methods, there are clear limitations for the structure assignments. For example, stereoisomers and some structural isomers cannot be distinguished.

Molecular Imaging. The imaging experiments were performed with a computer-controlled, stepper motor-driven, three-axis precision flexure stage (NanoMax TS, Thorlabs, Newton, NJ). The flexure stage with additional piezoelectric actuators and displacement sensors had a travel range of 4 mm, a theoretical resolution of 25 nm, and a repeatability of 1 μm. The sample surfaces mounted on the flexure stage were scanned in front of the mass spectrometer inlet orifice. The mass spectra obtained at each spot exposed to the laser beam (pixel) were averaged, typically for 50 laser pulses, and stored as a function of scanning time. Two-dimensional spatial distributions of the ion intensities were recovered from the ion chromatograms by a LabView program. A scientific visualization package (Origin 7.0, OriginLab Co., Northampton, MA) was used to produce false color images representing ion abundances as a function of position.

Materials and Sample Preparation. Various plant organs including flowers (white lily, *Lilium candidum*), fruits (banana, *Musa paradisiaca*, and tomato, *Solanum lycopersicum*), aggregate fruits (strawberry, Fragaria ananassa), leaves (cilantro, *Coriandrum sativum*, and peace lily, *Spathiphyllium*), tubers (potato, *Solanum tuberosum*), bulbs (onion, *Allium cepa*, and garlic, *Allium sativum L.*), and seeds (almond, *Prunus amygdalus*) were obtained from a local supermarket. Except for the leaves and the flower petals that were studied without sectioning, tissue sections of 0.2−0.5 mm in thickness were prepared at room temperature with a scalpel, and without further treatment, they were carefully placed onto the sample stage. The wet tissue sections adhered to the sample holder through surface forces, whereas the samples with dry surfaces were attached with a double-sided tape.

RESULTS AND DISCUSSION

Laser Ablation of Plant Tissue. To test the damage induced by the laser, the lamina of a peace lily leaf was mounted on a target plate and exposed to laser pulses that produced 0.27 ± 0.03 J/cm^2 fluence in the elliptical focal area. Scanning electron microscope investigation of the interrogated area indicated the removal of the cuticle, the upper epidermis, part of the mesophyll, and the vascular bundles. Figure 1a shows the ablated area on a peace lily leaf after a single laser pulse. The tissue damage is localized to an elliptical area (due to the 45° angle of incidence) with 180 and 640 μm for the small and large axes, respectively. The top waxy cuticle layer and part of the upper epidermal cells were removed, but no damage to the underlying tissue was apparent. Upon exposure to six laser pulses, the laser crater became slightly larger (230 μm by 720 μm) and some of the

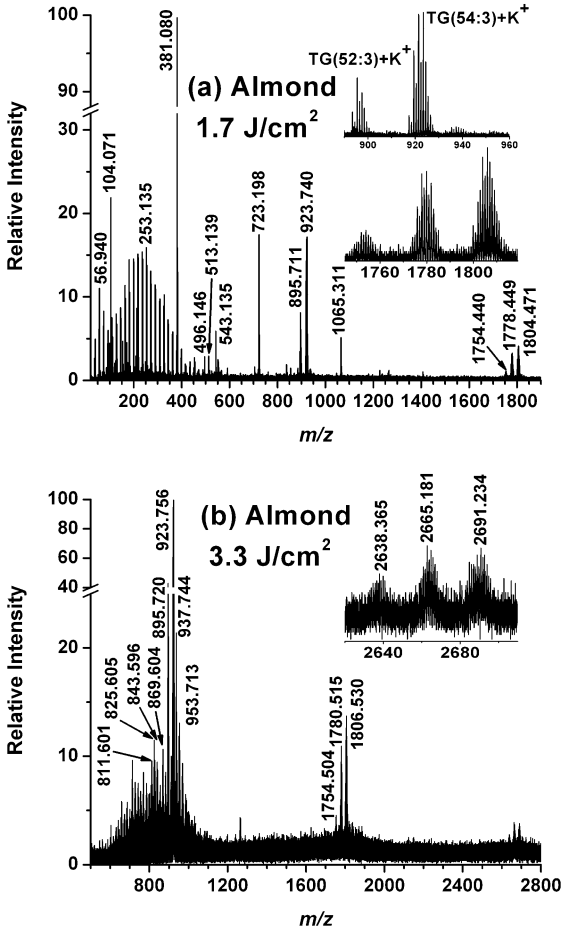

Figure 3. AP IR-MALDI mass spectra collected from the longitudinal section of an almond kernel for (a) low fluence (1.7 J/cm^2) and (b) high fluence (3.3 J/cm^2) exposures. The top inset in panel a shows triacylglrylcerol lipid distributions TG(52:4) to TG(52:2) and TG(54:6) to TG(54:3). The bottom inset in panel a zooms in on the potassiated dimers from these lipids. The inset in panel b indicates the formation of lipid trimers at elevated fluences.

palisade and spongy mesophyll was also removed (see Figure 1b). The opening visible close to the center of the crater appears to be a stoma essential in the gas exchange of the leaf. Overall, it seemed the damage caused by the laser was localized with a fairly well-defined boundary and, in case of probing individual points, did not interfere with the viability of the plant. The vicinity of the ablation crater did not show the redeposition of ablated material. From the analytical and especially from the imaging point of view, this was advantageous because it lowered the risk of point-to-point cross-contamination. The multiple-exposure case indicated that the consecutive laser pulses sampled increasing depths through the gradual removal of the tissue.

Mass Spectrometry. To survey the range of detected metabolites, tissue sections were prepared from plant organs of various species and positive (see Figures 2 and 3) and negative ion AP IR-MALDI spectra (see Figure 4) were recorded. Figures 2 and 4 compare different plant organs in positive and negative modes, respectively, whereas Figure 3 contrasts low fluence (1.7 J/cm^2 in panel a) and high fluence (3.3 J/cm^2 in panel b) spectra from the same sample. We collected spectra from sections of the outer wall of the pericarp of a tomato fruit (Figure 2d); a segment of a white lily flower petal (Figures 2c and 4c); the storage tissue in the outer medulla section of potato tubers (Figure 4a); ground tissue in the cross section of banana fruit; onion (Figure 4b) and garlic bulb (Figure 2b) sections that exposed the storage tissue in the expanded leaf bases; the cortex of a strawberry aggregate fruit containing several achenes and part of the accessory tissue of the receptacle; the lamina of a cilantro leaf (Figure 2a); and a longitudinal section of an almond kernel (Figures 3a and b, and 4d). Tandem mass spectrometry results for selected ions are shown in the insets of Figures 2b, and 4a and c. The tentative chemical assignments of the peaks, based on the methods outlined in the previous subsection, for the positive and the negative ion spectra are listed in Tables 1 and 2, respectively. Selected metabolic pathways for each compound are also indicated in both tables. In the following subsections, we discuss the observed ions grouped according to major primary and secondary metabolite compound groups.

(a) Carbohydrates and Oligosaccharide Synthesis. Over 30 peaks were observed in the AP IR-MALDI mass spectra of most samples with cationized carbohydrates, important primary metabolites, prominent in most them. For example, the potassiated sucrose ion with m/z 381.077 was observed for all of the organs and all the species. In the mass spectra of tuber, fruit, and bulb tissues, this ion produced the most abundant peak, indicating high sucrose content. Sucrose is the major product of photosynthesis in plants and the dominant form in which carbohydrates are transferred from the leaves to the rest of the plant, to supply carbon and energy for growth and the accumulation of storage reserves. At m/z 365.106, the sodiated sucrose ion was also observed with lower intensity, consistent with the lower concentration of sodium than potassium in these tissues.

With the exception of spectra from potato tuber and garlic bulb tissues, another abundant ion was observed at m/z 219.028 corresponding to the potassiated hexose sugars ($[C_6H_{12}O_6 + K]^+$). In addition to the accurate mass value (4 ppm mass accuracy), the presence of potassium in this ion was also confirmed by the isotope pattern (see the inset in Figure 2d). As mentioned in the Experimental Section, the elevated relative intensity of the $[M + 2]^+$ at the nominal m/z 221 ion relative to the abundance of $[M + 1]^+$ at m/z 220 was consistent with the natural contribution of the ^{41}K isotope.

In the positive ion spectra, the formation of oligosaccharides ($C_{6n}H_{10n+2}O_{5n+1}$) was detected up to $n = 5$ through the presence of tri-, tetra-, and pentasaccharides (e.g., raffinose, stachyose, and verbascose, respectively) in bulbs and for the trisaccharides in fruits and seeds. In bulbs, starting from α-D-fructofuranose β-D-fructofuranose 1,2′:1,2′-dianhydride ($C_{12}H_{20}O_{10}$), a series of fructans with a formula of $(C_6H_{10}O_5)_n$ was identified up to $n = 7$. These species could be produced through hexose condensation to the dianhydrade or for $n = 4$ and larger molecules through macrocycle formation (e.g., cyclomaltodextrin, $C_{18}H_{30}O_{15}(C_6H_{10}O_5)_n$). A quantitative measure for the reliability of the peak assignments was expressed by the absolute deviation of measured and calculated monoisotopic mass values, Δm expressed in millidaltons. In this respect, all the carbohydrate assignments above were accurate within $\Delta m < \pm 7$ mDa. In some spectra, phosphorylated (m/z 261.053 and 268.948) and aminosugars (m/z 196.048) were also identified, although the fidelity of these assignments ($\Delta m <$

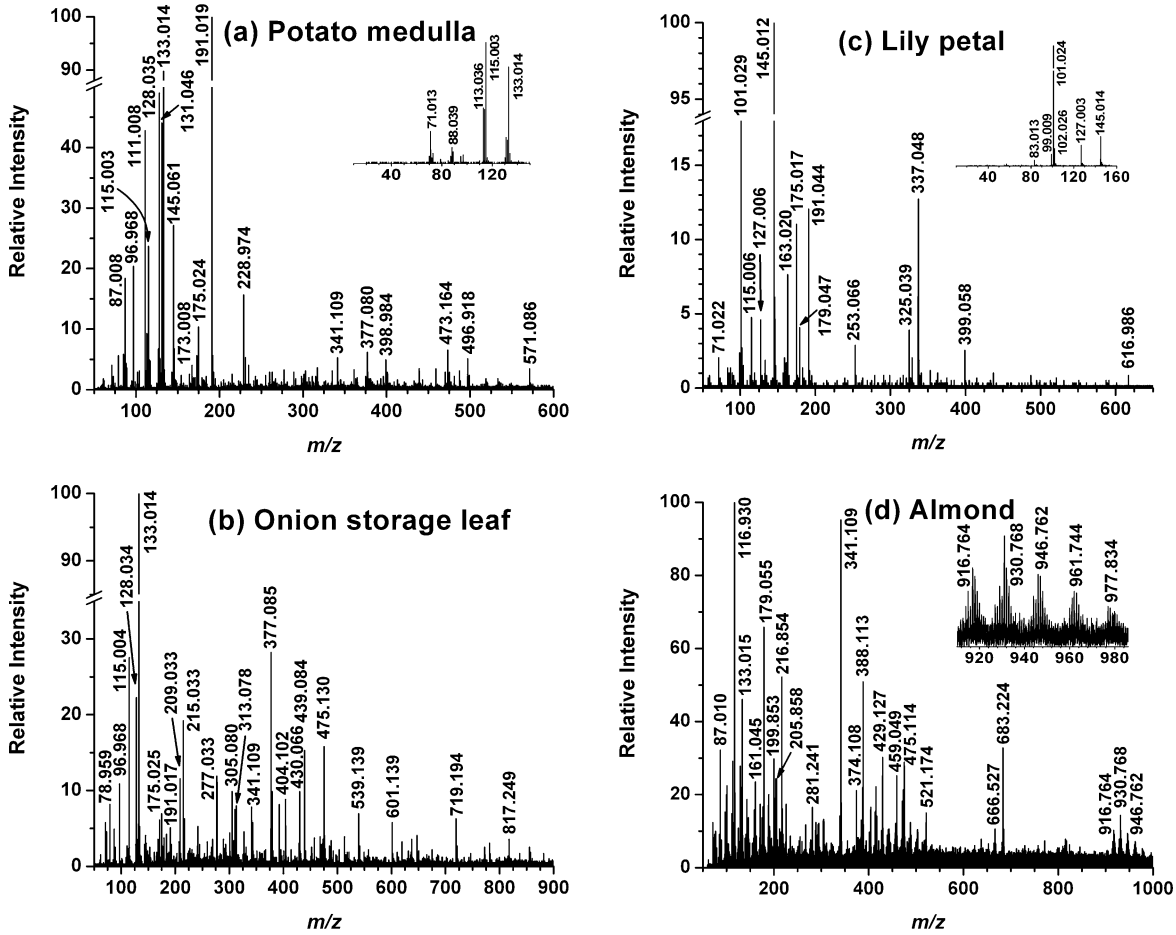

Figure 4. AP IR-MALDI mass spectra obtained in the negative ion mode for (a) the storage tissue in the outer medulla section of potato tubers, (b) onion storage leaf; (c) a segment of a white lily flower petal, and (d) a longitudinal section of an almond kernel. The insets in panels a and c are the tandem mass spectra of the ions with *m*/*z* 133 and 145 that are identified as malic acid and α-ketoglutaric acid, respectively. The inset in panel d depicts the zoomed triacylglrlycerol lipid distributions starting from TG(54:6).

±35 mDa) was lower than that for the carbohydrates discussed above.

Due to the high abundance of hexose and sucrose in fruits, extensive clustering of these species was observed in the form of potassiated hexose dimers and sucrose dimers, trimers, and tetramers. In the negative ion spectra, hexose, sucrose, their clusters, and some mixed clusters with other molecules (water, small organic acids, and aliin) appeared through proton loss. Although due to reducing sensitivity, clustering is generally regarded as detrimental to mass spectra in this study the cluster ions served as valuable internal standards and helped to maintain the accuracy of the mass scale.

(b) Amino Acids. Amino acids were the second large group of observed primary metabolites. They appeared prominent in both the positive and negative ion spectra through cationization and proton loss, respectively. Glutamine, lysine, histidine, asparagine, and arginine in the positive ion mode were identified with $\Delta m <$ ±3 mDa, whereas asparagine, aspartic acid, glutamine, glutamic acid, and histidine were observed in the negative ion spectra with $\Delta m <$ ±1 mDa accuracy. The excellent mass accuracy in combination with the knowledge of the metabolic role of these compounds verified by their presence in the Arabidopsis database provided strong reinforcement in their assignment. For example, the distinction of glutamine and lysine is usually problematic as both produce protonated molecular ions at nominal m/z 147. There is, however, a calculated $\Delta m = 36$ mDa difference in their monoisotopic masses. The accuracies for the measured glutamine and the lysine protonated ion m/z values were $\Delta m = 3$ and 1 mDa, respectively; thus, these amino acids could also be distinguished.

The inset in Figure 2b shows the tandem MS of the m/z 175.120 ion from garlic clove tissue. Based on accurate mass measurements, we assigned it as protonated arginine with a $\Delta m <$ ±1 mDa accuracy. Comparison of the tandem mass spectrum in the inset with the NIST/EPA/NIH Mass Spectral Library revealed strong similarity with MS/MS fragmentation of protonated arginine through the presence of fragments with nominal m/z 175, 158, 130, 116, 112, 88, 72, 70, and 60. Although the peak intensities in the library spectrum were different from the ones we observed, the almost complete agreement of the fragmentation patters provided yet another peice of evidence for the assignment of the parent ion.

In the negative ion spectra of glutamine, the deprotonated molecular ion with m/z 145.061 could be identified based on the good agreement with the calculated monoisotopic value of m/z 145.0613. In flower petals, however, there was a very abundant ion within $\Delta m = 49$ mDa. To further elucidate the structure of the $[M - H]^-$ ion, CAD was performed to produce the tandem

Table 1. Peak Assignments in Positive Ion Mass Spectra of Plant Organs

observed *m/z*	exact *m/z*	Δ*m* (mDa)	ion	plant organs[a]	metabolic pathways[b]
104.071[c]	104.0711	0	γ-aminobutyric acid + H^+	BU, FL, FR, SE, TU	arginine degradation, glutamate degradatio
138.056	138.0555	+1	2-aminobenzoic acid + H^+	FR	tryptophan biosynthesis
			4-aminobenzoic acid + H^+	FR	tetrahydrofolate biosynthesis
142.027[c]	142.0270	0	γ-aminobutyric acid + K^+	FR, TU	arginine degradation, glutamate degradation
147.080	147.0770	+3	glutamine + H^+	FR	arginine, asparagine, histidine and tryptophan biosynthesis, *de novo* biosynthesis of purine nucleotides
147.114	147.1134	+1	lysine + H^+	BU	lysine biosynthesis and degradation and methionine salvage pathway
156.078	156.0773	+1	histidine + H^+	FR	histidine biosynthesis and methionine salvage pathway
169.029	169.0267	+2	2-oxoisocaproic acid + K^+	FR	leucine biosynthesis and degradation
			2-oxo-3-methylvaleric acid + K^+	FR	
171.017[c]	171.0172	0	asparagine + K^+	LE, TU	asparagine biosynthesis and degradation and methionine salvage pathway
175.121[c]	175.1195	+2	arginine + H^+	BU, FR, LE, TU	arginine biosynthesis and degradation, methionine salvage pathway
185.032[c]	185.0328	−1	glutamine + K^+	FL, LE	arginine, asparagine, histidine and tryptophan biosynthesis, *de novo* biosynthesis of purine nucleotides
185.034	185.0328	+1	glutamine + K^+	FR, TU	
196.048	196.0821	−34	glucosaminic acid + H^+	BU	glucosamine metabolism
	196.0834	−35	6-hydroxymethyl-dihydropterin + H^+	BU	tetrahydrofolate biosynthesis
208.967[c]	208.9617	+5	dihydroxy-acetone-phosphate + K^+	TU, LE	Calvin cycle, glycolysis I and II and sucrose degradation
			D-glyceraldehyde-3-phosphate + K^+	TU, LE	Calvin cycle, glycolysis I and II and sucrose degradation
213.074[c]	213.0754	−1	arginine + K^+	BU	arginine biosynthesis and degradation, methionine salvage pathway
219.028[c]	219.0271	+1	hexose sugars + K^+	BU, FL, FR, LE	sucrose degradation and starch degradation
222.990	222.9774	+13	3,4-dihydroxy-2-butanone-4-phosphate + K^+	FL, TU	flavin biosynthesis
230.993[c]	230.9907	+2	citric acid + K^+	FR	citric acid cycle
253.965	253.9594	+6	erythronate-4-phosphate + K^+	BU	pyridoxal 5'-phosphate biosynthesis
261.053	261.0375	+16	D-fructose-6-phosphate + H^+	LE	glycolysis I and II
268.948[c]	268.9828	−35	D-ribose-5-phosphate + K^+ and/or D-ribulose 5-phosphate + K^+ and/or D-xylulose 5-phosphate + K^+	FR	Calvin cycle, non-oxidative branch of the pentose phosphate pathway
293.067[c]	293.0639	+3	β-D-galactopyranosyl-1-glycerol+K^+	FL	monogalactosylglycerol precursor
295.133[c]	295.1100	+23	4,9,13-trimethyltetradeca-2,4,6,-8,10,12-hexaene- 1,14-dial + K^+	FR	sphingolipid metabolism
322.090	322.0554	+35	guanosine + K^+	FR	purine degradation
	322.0904	0	γ-aminobutyric acid + hexose sugar + K^+	FR	cluster
329.058	329.0427	+15	2,3-*trans*-catechin and/or 2,3-*cis*-epicatechin + K^+	BU	proanthocyanidin biosynthesis from flavanols
	329.0540	+4	indole-3-acetyl-aspartic acid + K^+	BU	indole-3-acetic acid conjugate biosynthesis
	329.0863	−28	argininosuccinic acid + K^+	BU	arginine biosynthesis
363.070	363.0693	+1	α-D-fructofuranose β-D-fructofuranose 1,2′:1,2′-dianhydride ($C_{12}H_{20}O_{10}$) + K^+	BU	fructan biosynthesis
365.106	365.1060	0	sucrose + Na^+	BU, FL	sucrose degradation and stachyose biosynthesis
381.077[c]	381.0799	−3	sucrose + K^+	BU, FL, FR, LE, SE, TU	sucrose degradation and stachyose biosynthesis
387.186	387.1574	+29	GA14, GA15, GA53, GA110 + K^+	BU	plant hormone
393.055[c]	393.0214	+34	5-amino-6-(5′-phosphoribosyl-amino)uracil + K^+	BU, TU	flavin biosynthesis
	393.0588	−4	chlorogenic acid + K^+	BU, TU	phenylpropanoid biosynthesis
399.090[c]	399.0905	0	2[hexose sugars] + K^+	BU, FL, FR	cluster
411.046	411.0846	−39	sesamolinol + K^+	FR	lignan biosynthesis
455.125	455.0815	+44	5'-phosphoribosyl-4-(*N*-succinocarb-oxamide)-5-aminoimidazole + H^+	FL	*de novo* biosynthesis of purine nucleotides
525.122	525.1222	0	fructan ($C_{18}H_{30}O_{15}$) + K^+	BU	fructan biosynthesis
527.149	527.1490	0	glutamine+sucrose + K^+	BU, FL	cluster
527.162	527.1588	+3	trisaccharides (e.g., raffinose) + Na^+	BU	stachyose biosynthesis
543.136[c]	543.1327	+3	trisaccharides (e.g., raffinose) + K^+	BU, FR, SE	stachyose biosynthesis
551.101[c]	551.1014	0	gallic acid+sucrose + K^+	TU	cluster

Table (Continued)

observed *m/z*	exact *m/z*	Δ*m* (mDa)	ion	plant organs[a]	metabolic pathways[b]
565.114	565.0836	+30	thymidine-diphosphate-D-glucose + H^+	TU	thymidine-diphosphate-L-rhamnose biosynthesis
	565.0936	+20	3,4-dihydroxy-2-butanone-4-phosphate + sucrose + K^+	TU	cluster
649.107	649.1171	−10	quercetin 3-*O*-rutinoside + K^+	LE	quercetin glucoside biosynthesis
			quercetin 3-*O*-rhamnoside-7-*O*-glucoside + K^+	LE	quercetin glucoside biosynthesis
			kaempferol 3,7-*O*-diglucoside + K^+	LE	kaempferol glucoside biosynthesis
687.175	687.1750	0	fructan ($C_{24}H_{40}O_{20}$) + K^+	BU	fructan biosynthesis
705.192	705.1855	+7	tetrasaccharides (e.g., stachyose) + K^+	BU	ajugose biosynthesis I
723.214	723.1961	+18	2[sucrose] + K^+	FR, SE, TU	cluster
796.549	796.5258	+23	18:1−18:1-phosphatidyl-ethanolamine + K^+	FL	phospholipid biosynthesis
849.231	849.2278	+3	fructan ($C_{30}H_{50}O_{25}$) + K^+	BU	fructan biosynthesis
867.241	867.2384	+3	pentasaccharides (e.g., verbascose) + K^+	BU	ajugose biosynthesis I
1011.278	1011.2807	−3	fructan ($C_{36}H_{60}O_{30}$) + K^+	BU	fructan biosynthesis
1065.308	1065.3123	−4	3[sucrose] + K^+	FR, SE	cluster
1173.331	1173.3335	−2	fructan ($C_{42}H_{70}O_{35}$) + K^+	BU	fructan biosynthesis
1407.432	1407.4285	+4	4[sucrose] + K^+	FR	cluster

[a] BU: bulb (garlic and onion); FL: flower (lily); FR: (banana, strawberry and tomato); LE: leaf (cilantro); SE: seed (almond); TU: tuber (potato); [b]This incomplete list was compiled through the AraCyc 3.5 database at http://www.arabidopsis.org/ for arabidopsis and the MetaCyc combined database for 261 organisms at http://biocyc.org/. [c]Tandem MS available.

mass spectrum (see the inset in Figure 4c). The dominant fragment ions with nominal *m/z* 127, 101, and 83 corresponded to neutral losses of H_2O, CO_2, and [H_2O + CO_2], respectively. Comparing this fragmentation pattern with the literature data[74] for the CAD of the glutamate ion revealed that the presence of the *m/z* 83 species was inconsistent with this assignment. Due to the presence of the two carboxyl groups in α-ketoglutaric acid, the loss of both CO_2 and H_2O was more likely from its $[M - H]^-$ ion. The accurate mass of this ion, *m/z* 145.012, was also convincingly close to the calculated *m/z* 145.0137.

(c) Organic Acids. The third group of metabolites observed in the spectra can be classified as organic acids. The positive ions with *m/z* 104.071, 138.056, 169.029, and 230.993 were assigned as cationized γ-aminobutyric acid (GABA), aminobenzoic acid, 2-oxoisocaproic acid, and citric acid, respectively. The mass accuracy of these assignments was within $\Delta m < \pm 2$ mDa.

In the negative ion spectra, the deprotonated forms of pyruvic acid (*m/z* 87.008), 2-furoic acid (*m/z* 111.008), fumaric acid (*m/z* 115.003), pyrroline-hydroxy-carboxylate (*m/z* 128.035), malic acid (*m/z* 133.014), α-ketoglutaric acid (*m/z* 145.012), aconitic acid (*m/z* 173.008), ascorbic acid (*m/z* 175.017), oxalosuccinic acid (*m/z* 189.002), citric acid (*m/z* 191.019), quinic acid (*m/z* 191.044), and 5-hydroxyferulic acid (*m/z* 209.033) were noted. The *m/z* 101.029 ion could be derived from α- or β-ketobutyric acid or succinic acid semialdehyde through proton loss. The peak assignments were within $\Delta m < \pm 12$ mDa the measured *m/z* values.

These small organic acids perform diverse roles as metabolites. For example, GABA is the product of arginine and glutamic acid degradation, but it is also believed to be involved in the regulation of plant development, as well as in defense and other stress responses.[75] Recent evidence from the functional genomic analysis of Arabidopsis indicates that GABA might also play a role as a signaling molecule.[76] Quinic acid is a key intermediate in the biosynthesis of aromatic compounds in living systems, whereas α-ketoglutaric acid is critical in enzyme systems, in the citric acid cycle and in the transamination process.[77] Another interesting example, deprotonated malic acid at *m/z* 133.014, was detected in nine different tissue samples. According to the Arabidopsis metabolic pathway database, malic acid is involved as a reactant in the glyoxylate cycle, sinapate ester biosynthesis, the superpathway of the glyoxylate cycle, and the citric acid cycle. It is produced in fatty acid ω oxidation, the glyoxylate cycle, glycolate and glyoxylate degradation, and the superpathway of the glyoxylate cycle. Malic acid also participates in a number of reactions without pathways. Organic acids act not only as intermediates in carbon metabolism but also as key components in the mechanism that some plants use to cope with nutrient deficiencies, metal tolerance, and plant−microbe interactions operating at the root−soil interphase.[78]

(d) Lipids. It required higher laser fluences to obtain mass spectra from almond seed tissue. Figure 3 compares the spectra at 1.7 J/cm^2 in panel a and 3.3 J/cm^2 in panel b. The need for higher fluence could be rationalized in terms of the lower water content of the seed tissue. In addition to the seed metabolites already described in Tables 1 and 2, typical lipid mass spectral patterns were observed in the vicinity of the most abundant *m/z* 895.711 and 923.740 ions. Comparison of these patterns with data from the LIPID MAPS database revealed the presence of unsaturated triacylglrycerol (TG) mixtures. For example, the *m/z* 895.711 peak was consistent with the potassiated TG(17:1(9Z)/17:1(9Z)/18:1(9Z)) with calculated monoisotopic *m/z* 895.7157. In reality, any combination of acyl chain lengths that added up to 52 and

(74) Kulik, W.; Heerma, W. *Biomed. Environ. Mass Spectrom.* **1988**, *15*, 419−427.
(75) Ma.H. *Curr. Biol.* **2003**, *13*, R834−836.
(76) Bouche, N.; Fromm, H. *Trends Plant Sci.* **2004**, *9*, 110−115.
(77) Yang, X.; Bi, S.; Wang, X.; Liu, J.; Bai, Z. *Anal. Sci.* **2003**, *19*, 273−279.
(78) Lopez-Bucio, J.; Nieto-Jacobo, M. F.; Ramirez-Rodriguez, V.; Herrera-Estrella, L. *Plant Sci.* **2000**, *160*, 1−13.

Table 2. Peak Assignments in Negative Ion Mass Spectra of Plant Organs

observed *m/z*	exact *m/z*	Δ*m* (mDa)	ion	plant organs[a]	metabolic pathways[b]
87.008	87.0082	0	pyruvic acid − H^+	BU, FR, LE, SE	glycolysis I
101.029[c]	101.0239	+5	α-ketobutyric acid − H^+	FL	isoleucine biosynthesis
			β-ketobutyric acid − H^+	FL	leucine degradation
			succinic acid semialdehyde − H^+	FL	arginine degradation
111.008[c]	111.0082	0	2-furoic acid − H^+	BU, FR, TU	reacts with coenzyme A
115.003[c]	115.0031	0	fumaric acid − H^+	BU, FL, FR, LE, TU	citric acid cycle
128.035[c]	128.0348	0	pyrroline-hydroxy-carboxylate − H^+	BU, FR, TU	redox agent, 4-hydroxyproline degradation
131.046	131.0457	0	asparagine − H^+	LE, TU	asparagine biosynthesis and degradation, methionine salvage pathway
132.029	132.0297	−1	aspartic acid − H^+	FR	aspartate biosynthesis and degradation, *de novo* biosynthesis of purine nucleotides
133.014[c]	133.0137	0	malic acid − H^+	BU, FL, FR, LE, SE, TU	citric acid cycle
145.012[c]	145.0137	−2	α-ketoglutaric acid − H^+	FL	citric acid cycle, alanine, arginine, asparagine, proline and serine biosynthesis, flavonoid biosynthesis, photorespiration
145.061[c]	145.0613	0	glutamine − H^+	FR, TU	arginine, asparagine, histidine and tryptophan biosynthesis and *de novo* biosynthesis of purine nucleotides
146.045[c]	146.0453	0	glutamic acid − H^+	FR, LE	aspartate biosynthesis and degradation
154.061	154.0617	−1	histidine − H^+	FR	methionine salvage pathway
173.008	173.0086	−1	aconitic acid − H^+	FR, TU	citric acid cycle
175.017	175.0243	−7	ascorbic acid − H^+	BU, FL, FR, LE, TU	ascorbate glutathione cycle and ascorbate biosynthesis
176.038[c]	176.0381	0	alliin − H^+	BU	glutathione degradation
179.055	179.0556	−1	hexose sugars − H^+	FL, FR, SE	sucrose degradation and starch degradation
189.002	189.0035	−1	oxalosuccinic acid − H^+	LE	citric acid cycle
191.019[c]	191.0192	0	citric acid − H^+	BU, FR, LE, TU	citric acid cycle
191.044	191.0556	−12	quinic acid − H^+	FL	phenylpropanoid biosynthesis
209.033	209.0450	−12	5-hydroxy-ferulic acid − H^+	BU	free phenylpropanoid acid biosynthesis
215.032[c]	215.0321	0	2-*C*-methyl-D-erythritol-4-phosphate − H^+	BU, FR	methyl erythritol phosphate pathway
253.066	253.0702	−4	arginine phosphate − H^+	FL	arginine and proline metabolism
277.033[c]	276.9878	+45	2-*C*-methyl-D-erythritol-2,4-cyclodiphosphate − H^+	BU, FR	methyl erythritol phosphate pathway
313.075	313.0606	+14	geranyldiphosphate − H^+	BU, FR	monoterpene biosynthesis
325.039	325.0437	−5	2,4-dioxotetrahydropyrimidine D-ribonucleotide − H^+	FL	pentose phosphate pathway, pyrimidine metabolism
326.110	326.1392	−29	*S*-scoulerine − H^+	FR	alkaloid biosynthesis
	326.1087	+1	glutamic acid + hexose sugar − H^+	FR	cluster
337.048[c]	337.0549	−7	aminoimidazole carboxamide ribonucleotide − H^+	FL	*de novo* biosynthesis of purine nucleotides I
	337.0407	+7	α-ketoglutaric acid + citric acid − H^+	FL	cluster
341.109[c]	341.1084	+1	sucrose − H^+	BU, FR, LE, SE, TU	sucrose degradation and stachyose biosynthesis
359.119[c]	359.1190	0	2[hexose sugars] − H^+	FR	cluster
377.080[c]	377.1295	−49	sucrose + 2[H_2O] − H^+	BU, FR, TU	cluster
475.135[c]	475.1299	+5	malic acid + sucrose − H^+	BU, FR, SE	cluster
518.154[c]	518.1544	0	alliin+sucrose − H^+	BU	cluster
521.170	521.1718	−2	hexose sugars + sucrose − H^+	FR, SE	cluster
533.129	533.1354	−6	citric acid + sucrose − H^+	BU, FR	cluster
683.224	683.2246	−1	2[sucrose] − H^+	FR, SE	cluster
719.203	719.2457	−43	2[sucrose] + 2[H_2O] − H^+	BU, FR	cluster
817.249	817.2461	+3	malic acid + 2[sucrose] − H^+	BU	cluster
875.257	875.2516	+5	citric acid + 2[sucrose] − H^+	FR	cluster

[a] BU, bulb (garlic and onion); FL, flower (lily); FR, (banana, strawberry and tomato); LE, leaf (cilantro); SE, seed (almond); TU, tuber (potato). [b] This incomplete list was compiled through the AraCyc 3.5 database at http://www.arabidopsis.org/ for arabidopsis and the MetaCyc combined database for 261 organisms at http://biocyc.org/. [c] Tandem MS available.

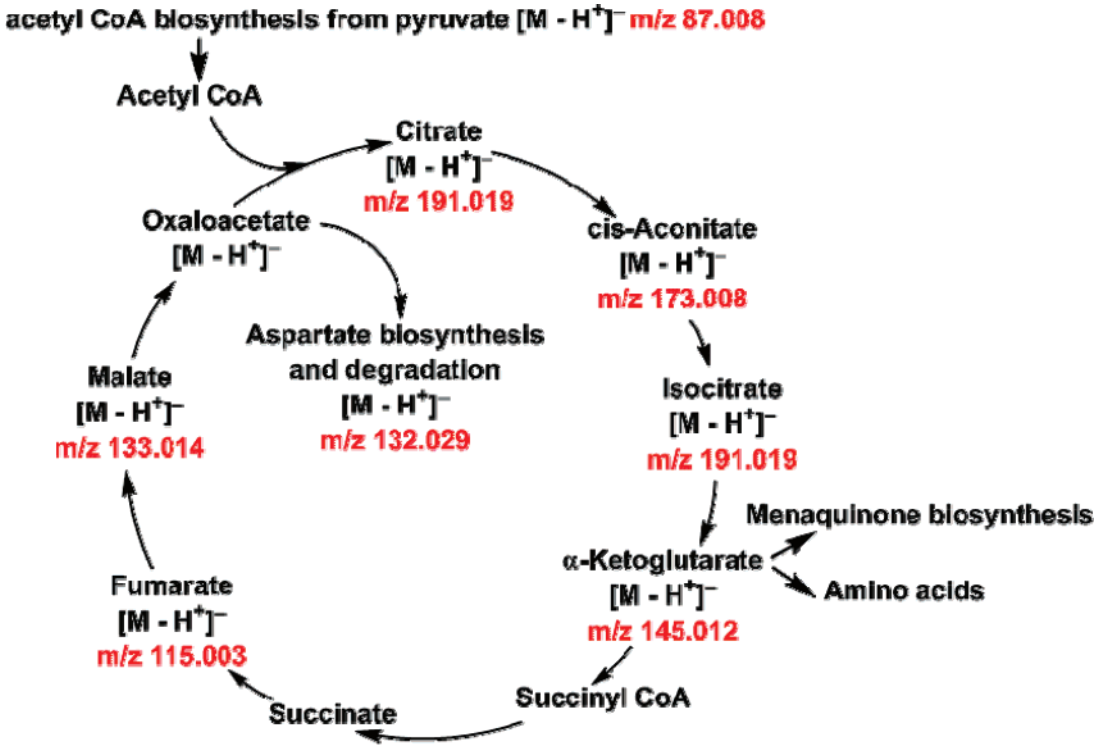

Figure 5. Major metabolites in the citric acid cycle. The species detected by AP IR-MALDI in this study are designated by the measured *m/z* values in the schematics.

any arrangement of the 3 double bonds along those chains would be consistent with the observed *m/z* within $\Delta m = -5$ mDa. To designate all possible structural isomers with the same *m/z*, this lipid can be denoted as TG(52:3). The neighboring peaks at *m/z* 893.7000 and 897.7313 corresponded to the potassiated TG(52:4) and TG(52:2) molecules, respectively. The lipid distribution was convoluted with the carbon isotope patterns for all three species. Similarly, the *m/z* 923.740 ion could be identified as potassiated TG(18:1(9Z)/18:1(9Z)/18:1(9Z)) along with all of its structural isomers. The calculated monoisotopic mass for this ion produced *m/z* 923.7469. The notation for all isomers of this species included was TG(54:3). The neighboring peaks were produced by a convolution of TG(54:4), TG(54:5), and TG(54:6) with the carbon isotope distribution patterns.

Three sets of peaks were observed at *m/z* 1754.440, 1778.449, and 1804.471. These three groups could be explained as potassiated lipid dimers. For example, mixing two of the lighter lipids, $[TG(52:2) + TG(52:3) + K]^+$ produced an *m/z* 1754.483 ion. Combining two heavier species, $[2TG(54:4) + K]^+$, resulted in *m/z* 1804.499, whereas dimers mixed from both the light and heavy group, $[TG(52:4) + TG(54:3) + K]^+$, produced *m/z* 1778.483. Further increasing the laser fluence to 3.3 J/cm^2 favored the formation of clusters. This is demonstrated in Figure 3b, where the intensity of dimer peaks is increased and the formation trimer patterns can be observed at *m/z* 2638.365, 2665.181, and 2691.234.

(e) Miscellaneous Metabolites. This is a diverse group that includes a few primary as well as secondary metabolites. Several nucleotides (thymidine diphosphate-D-glucose, 2,4-dioxotetrahydropyrimidine D-ribonucleotide and aminoimidazole carboxamide ribonucleotide), and a nucleoside (guanosine), various phosphates (dihydroxyacetonephosphate, erythronate-4-phosphate, arginine phosphate, 2-C-methyl-D-erythritol-4-phosphate, 2-C-methyl-D-erythritol-2,4-cyclodiphosphate, and geranyl diphosphate), an amino acid derivative (alliin in garlic), and lipid-related compounds (β-D-galactopyranosyl-1-glycerol and 18:1−18:1-phosphatidylethanolamine) were found. Among the secondary metabolites, we assigned some flavonoids and flavonoid precursors (e.g., quercetin 3-*O*-rutinoside, and 3,4-dihydroxy-2-butanone-4-phosphate), plant hormones (GA14, GA15, GA53, and GA110), a lignan (sesamolinol), and a precursor of lignin biosynthesis (chlorogenic acid).

The Δm values in Tables 1 and 2 indicate that some of these assignments are characterized by lower mass accuracy. The worst value was found for 5′-phosphoribosyl-4-(*N*-succinocarboxamide)-5-aminoimidazole with $\Delta m = +44$ mDa or 97 ppm in relative terms. In some cases, several compounds were within acceptable range, so unique assignments were not made. For example, the *m/z* 329.058 peak could be produced by potassiated 2,3-*trans*-catechin ($\Delta m = +15$ mDa), indole-3-acetylaspartic acid ($\Delta m = +4$ mDa), or argininosuccinic acid ($\Delta m = -28$ mDa) molecules. More reliable assignments in such cases can be established by tandem MS investigation of the ion or from an internal calibration of the spectrometer that exhibits more accuracy in the *m/z* region of interest. In the present study. we did not pursue these objectives.

Cellular Respiration Reflected by AP IR-MALDI. The considerable amount of data obtained by AP IR-MALDI and the broadening array of metabolomics databases enabled us to identify several components of major metabolic pathways, in some cases with good coverage. Depending on how many intermediates are included, the citric acid or tricarboxylic acid (TCA) cycle can be depicted as a cycle of 8−10 reactions that are important in C2−C4 interconversion and energy production and lie at the intersection of catabolic and anabolic pathways. Figure 5 depicts the citric acid cycle, a central step in aerobic cellular respiration. This view

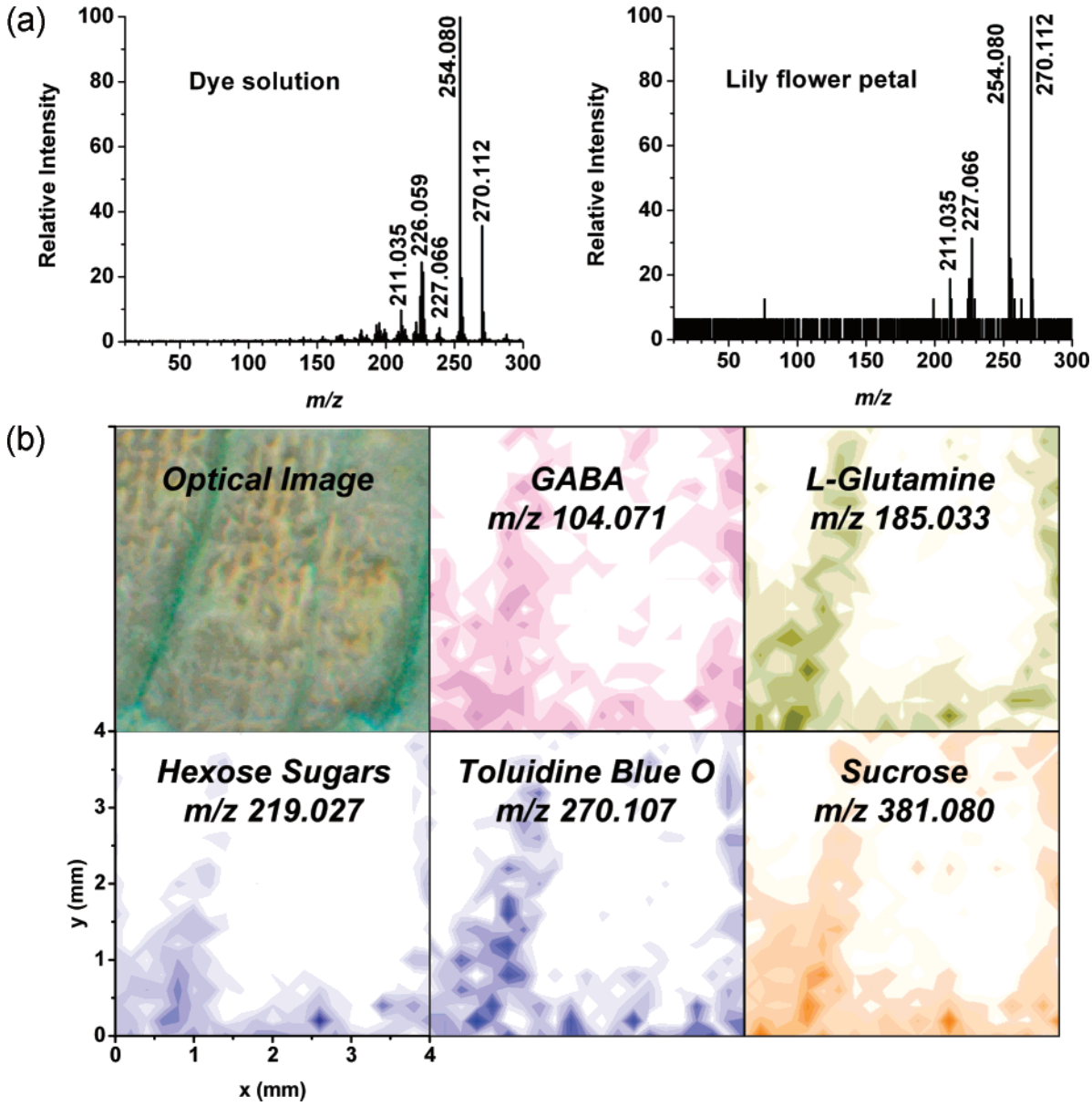

Figure 6. (a) Comparison of the tandem mass spectra of the nominal *m*/*z* 270 ion observed in the AP IR-MALDI mass spectra of toluidine blue O dye solution (left panel) and white lily flower petal after 48 h (right panel). (b) Optical and AP IR-MALDI images of the white lily flower petal section stained in the fluid transport experiment. Spatial distributions of GABA, glutamine, hexose sugars, toluidine blue O, and sucrose in the petal show a higher concentration of nutrients and metabolites in the vasculature.

shows nine intermediates in the form of organic acid anions. The *m*/*z* values in the figure indicate the deprotonated molecules actually detected in the AP IR-MALDI spectra. Inspecting Table 2 confirmed that six of the components within the cycle—citrate/isocitrate, aconitate, α-ketoglutarate, fumarate, and malate—and two additional closely related species—pyruvate and aspartate—were detected with an accuracy of $\Delta m \leq 2$ mDa. It should be noted that the citrate and isocitrate were indistinguishable in the AP IR-MALDI spectra. In the extended version of the TCA cycle, the oxalosuccinate intermediate is found between the isocitrate and the α-ketoglutarate. We also detected this anion in the negative ion spectra within the accuracy limit indicated above. Thus, the metabolite coverage of the citric acid cycle by AP IR-MALDI was 70%.

Other metabolic pathways were covered to a much lower degree. Glycolysis, the precursor of the TCA cycle in the cellular respiration process, was only represented by glucose (detected in the form of potassiated hexose), D-fructose 6-phosphate, dihydroxyacetone phosphate/D-glyceraldehyde 3-phosphate (indistinguishable based on their *m*/*z* only), and pyruvic acid. Thus, of the 10 metabolites of the glycolysis I pathway, occurring in the plant cytosol, only 5 were detected and 4 distinguished based on *m*/*z* measurements alone. Further insight into the structure of these species could be obtained from tandem MS measurements.

Intermediates in additional pathways, such as the Calvin cycle, instrumental in carbon fixation, amino acid biosynthesis and degradation, nucleotide synthesis, flavonoid biosynthesis, lipid metabolism, and oligosaccharide biosynthesis and degradation were identified with good fidelity. Although the coverage of these pathways was low, efforts to target some of them could probably turn up more of the related molecules.

Metabolic Imaging and Fluid Transport Induced by Plant Transpiration. The stability of the AP IR-MALDI signal and the obtained ion intensities enabled us to perform imaging experiments on plant tissues. To produce a known chemical contrast, the cut end of a white lily plant stem was immersed into toluidine blue O dye solution (1 drop of 1% dye solution in 200 mL of deionized water). In 48 h, probably due to the presence of the toluidine blue dye or its metabolite, a visual observation of the originally white flower petals indicated light blue discoloration. Correspondingly, a positive ion with m/z 270.112 was observed in the AP IR-MALDI mass spectrum, very close to the monoisotopic m/z 270.1065 calculated for the organic cation of the toluidine blue O salt. To further confirm the identity of this species, tandem AP IR-MALDI mass spectra of the nominal m/z 270 ion produced from the dye solution and from the flower petal were compared (see Figure 6a). The good agreement between the two fragmentation patterns supported the assignment of the m/z 270.112 ion from the flower petal as the toluidine blue O cation. This further confirmed the visual observation that the blue dye was absorbed by the plant stem and transported to the flower petals by the transpirational pull.

A 10×20 mm^2 section of the flower petal was removed and transferred onto the target plate for the imaging experiment. A coarse array of 21×21 pixels was used for AP IR-MALDI imaging with the dwell time and scanning step size set to 5 s and 200 μm, respectively. The image acquisition was completed in under 45 min.

Figure 6b shows the optical image of the lily flower petal after the imaging experiment along with the distributions of GABA, glutamine, hexose sugars, toluidine blue O, and sucrose. Close inspection of the stained flower petal under the optical microscope revealed that the dye concentration was higher in the vasculature. The primary and secondary veins in the petal appeared to be stained stronger, and this, observation was reflected in the optical image (top left panel in Figure 6b). Correspondingly, the distribution of toluidine blue O molecules indicated higher concentrations in the vasculature. The blue color in the optical image and the toluidine blue O distribution reflected by AP IR-MALDI appeared to be highly correlated. Somewhat lower, but still strong spatial correlation was observed for the nutrients (sucrose and hexose) as well as for the other two metabolites (GABA and glutamine). Indeed, it is known that these components are transported and distributed in the plant by the phloem within the vascular bundle. The correlation between the vascular architecture and nutrient availability within a plant had been demonstrated by observing isotope and dye distributions.[79] This so-called sectoriality has far-reaching implications for plant development and even ecology.

The spatial resolution in the molecular image is not sufficient to discern details on the cellular level. This limitation, however, can be resolved by tighter focusing of the laser beam. To obtain smaller focal spots, a shorter focal length focusing lens is needed and the laser beam divergence has to be reduced. This latter can be achieved by using a beam expander. Further improvement can be expected from taking advantage of aspherical optics.

CONCLUSIONS

In this paper, we demonstrated that AP IR-MALDI mass spectrometry can serve as an effective tool for quick identification of a wide array of metabolites, including simple carbohydrates, oligosaccharides, amino acids, organic acids, lipids, and a variety of other compounds, in plant tissues. We showed examples of detecting intermediates in the citric acid cycle (with 70% coverage) and in a variety of other metabolic pathways. As the analysis does not require extensive sample preparation and it can be performed at atmospheric pressure, AP IR-MALDI is ideally suited for the mass spectrometric analysis of living organisms. We also demonstrated the ability of this method to follow fluid transport induced by plant transpiration and to image molecular distributions in plant tissue.

Although the identification of ions was facilitated by both positive and negative ion spectra, generally high-mass accuracy and, in some cases, tandem mass spectrometry, the typical uncertainties of structure identification through mass spectrometry were present. For example, to reduce the structural ambiguity of the TG lipids, extensive tandem MS work would be necessary.

Importantly, exploring the quantitation capabilities of the method requires further work. In a previous publication,[42] we showed that close to the detection limit the AP MALDI response for mock liquid samples was semiquantitative with a dynamic range of 2 orders of magnitude. To further improve the utility of this technique for metabolomics, reliable quantitation of endogenous species in tissue samples has to be demonstrated. For example, the absolute concentrations for a wide array of metabolites (carbohydrates, amino acids, phosphorylated intermediates, etc.) in developing potato tubers are available from GC/MS measurements on nonaqueous tissue extracts.[80] A comparative study of metabolite quantitation in potato tuber tissue with AP IR-MALDI could help to establish these important figures of merit.

In the previous section, we indicated that the spatial resolution of AP IR-MALDI imaging can be significantly improved by better focusing. There are two related limitations of the instrumentation that need to be resolved simultaneously with the implementation of improved optics. First, to be able to collect images in a reasonable time, the repetition rate of the mid-IR laser has to be higher. The current 10-Hz repetition rate does not allow substantially increase in the dimensions of the image. At the same time, with the reduced laser spot size the sampled volume and consequently the mass spectrometric signal diminishes. This obstacle needs to be addressed through improved ion yields and better AP interface design.

An unexplored aspect of AP IR-MALDI is its potential for depth profiling in biological systems. Comparing Figure 1a and b shows how consecutive laser pulses sample deeper and deeper layers of the tissue. To take advantage of this capability, the removal rates of various tissues through laser ablation have to be established. This work can in part rely on the extensive data available for laser surgery applications. Indeed, ultimately the AP IR-MALDI chemical sampling can be combined with laser surgery. The analytical technique could be used to accurately monitor the removal of abnormal tissue through the mass spectrometric analysis of the ablated plume.

(79) Orians, C. M.; Ardon, M.; Mohammad, B. A. *Am. J. Bot.* **2002**, *89*, 270−278.

(80) Farre, E. M.; Tiessen, A.; Roessner, U.; Geigenberger, P.; Trethewey, R. N.; Willmitzer, L. *Plant Physiol.* **2001**, *127*, 685−700.

There are diverse potential applications for AP IR-MALDI in the life sciences. For example in plant biology, AP IR-MALDI imaging can be utilized to follow metabolism changes in genetically modified plants. In plant physiology experiments, the plant metabolic response to stress, such as starvation or drought conditions, can be monitored. In plant ecology, the understanding of plant−herbivore and plant−insect interactions can be facilitated by AP IR-MALDI mass spectrometry.

ACKNOWLEDGMENT

The authors are grateful for the support of this work by the W. M. Keck Foundation (041904), the US Department of Energy (DEFG02-01ER15129), and the George Washington University Research Enhancement Fund. Modified capillary inlets for this research were kindly provided by D. Kenny and the Waters Co. B.S. is grateful to B. N. Walker and J. Stolee for helping with taking the SEM images.

Received for review August 11, 2007. Accepted October 25, 2007.

AC701703F